

MEDICAL IMAGE REGISTRATION USING OPTIMAL CONTROL OF A LINEAR HYPERBOLIC TRANSPORT EQUATION WITH A DG DISCRETIZATION

BASTIAN ZAPF*, JOHANNES HAUBNER†, LUKAS BAUMGÄRTNER‡, AND STEPHAN SCHMIDT§

Key words. Image Registration, Image Transport, Optimization, Hyperbolic PDEs, Discontinuous Galerkin, Meshing

AMS subject classifications. 35D30, 35L02, 35Q49, 35Q93, 35R30, 49M05, 49M41, 49N45, 65D18, 65K10, 65M32, 65M50, 68T99

Abstract. Patient specific brain mesh generation from MRI can be a time consuming task and require manual corrections, e.g., for meshing the ventricular system or defining subdomains. To address this issue, we consider an image registration approach. The idea is to use the registration of an input magnetic resonance image (MRI) to a respective target in order to obtain a new mesh from a high-quality template mesh. To obtain the transformation, we solve an optimization problem that is constrained by a linear hyperbolic transport equation. We use a higher-order discontinuous Galerkin finite element method for discretization and show that, under a restrictive assumption, the numerical upwind scheme can be derived from the continuous weak formulation of the transport equation. We present a numerical implementation that builds on the established finite element packages FEniCS and dolfin-adjoint. To demonstrate the efficacy of the proposed approach, numerical results for the registration of an input to a target MRI of two distinct individuals are presented. Moreover, it is shown that the registration transforms a manually crafted input mesh into a new mesh for the target subject whilst preserving mesh quality. Challenges of the algorithm with the complex cortical folding structure are discussed.

1. Introduction. The availability of high quality meshes is a crucial component in the recent development of novel medical imaging analysis. For instance, open source high performance solver frameworks for partial differential equations (PDEs) have in recent years refined the understanding of the fundamental physiological processes governing molecular transport in the human brain [41]. Among other examples [45, 5, 33, 74, 72] have combined PDE-constrained optimization and medical resonance images (MRI) to study molecular transport on the macroscopic scale in the human brain. One major challenge in this modelling workflow is the generation of patient-specific meshes. To address this issue, [52] recently published a recipe on how to obtain a finite element mesh of a human brain based on a MR image. The accompanying software [73] uses brain surface files generated by FreeSurfer [27] and creates volume meshes using CGAL [69]. These semi-automatically generated meshes are useful for modeling of processes in the brain parenchyma as in [17, 63, 6].

However, in some applications like modelling of fluid transport in the cerebral aqueduct and the ventricular system [34, 11] manual mesh processing is required. This is a time-consuming task, which requires domain expertise and hence is hardly reproducible. In this work, we aim to simplify this workflow for future studies on new patients by utilizing manually crafted meshes to automatically generate new meshes from images.

Assume we are given two brain MRI scans from two different patients or the same patient at different times. Moreover, assume that we have obtained – in a time consuming process that required manual corrections – a mesh for some brain regions from the first MRI. The question that we address is how to obtain a mesh that fits to the second MRI using the existing mesh as input.

A similar question has recently been addressed in [38] using an affine transformation to a reference mesh. In comparison, our approach is based on nonlinear image registration and related to [43], where FreeSurfer registration was combined with large deformation diffeomorphic metric mappings [4]. In detail, we first use an affine registration followed by a nonlinear registration via (a sequence of) deformation velocity fields. The resulting transformation is then applied to transform the input mesh. The proposed methodology is demonstrated using actual human MRI data. The subjects are called “Abby” and “Ernie” and are publicly available at [51]. This idea is sketched in Fig. 1. Defining the transformation via velocity fields and at the same time ensuring that the mesh quality is preserved, implies that the two brain meshes have the same topology. Our approach to generate meshes from a new image hence implicitly requires the two brains to have the same topology. Hence, our approach naturally exploits the above mentioned requirement of no topological changes. We assume this to

*Department of Mathematics, University of Oslo, Oslo, Norway (bazapf@math.uio.no)

†Department of Numerical Analysis and Scientific Computing, Simula Research Laboratory, Oslo, Norway; Institute of Mathematics and Scientific Computing, University of Graz, Austria (johannes.haubner@uni-graz.at)

‡Institut of Mathematics, Humboldt University of Berlin, 10099 Berlin, Germany (lukas.baumgaertner@hu-berlin.de)

§Department of Mathematics, University of Trier, 54296 Trier, Germany (s.schmidt@uni-trier.de)

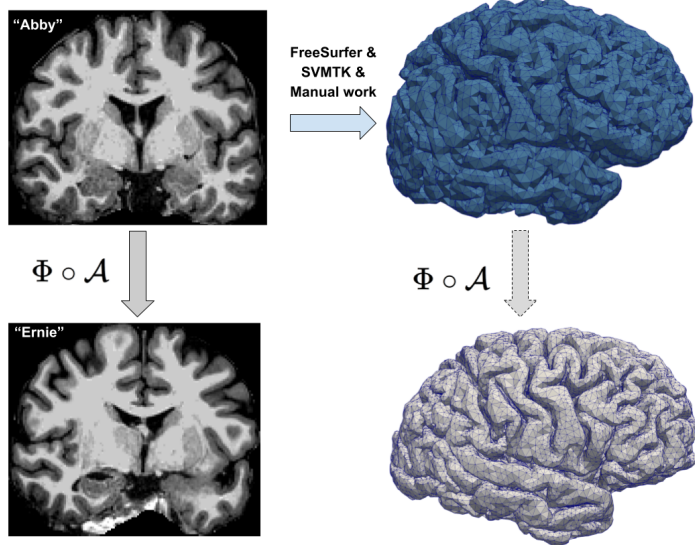


FIGURE 1. Sketch of the proposed mesh deformation pipeline to generate a mesh for target “Ernie” from an existing mesh for “Abby”. After optimizing a sequence of affine transformation \mathcal{A} and nonlinear deformations Φ that register the MRI from “Abby” to “Ernie”, the same transformation is applied to the mesh for “Abby”.

be valid in the given subject data and can otherwise be achieved by registering certain subregions individually.

Nonlinear registration, which is an essential part of this procedure, is a big field and not all relevant publications can be cited in this work. For a broader overview and introduction, we refer to, e.g., [9, 53, 49]. Medical image registrations have been reviewed in, e.g., [67, 57]. An experimental evaluation of different nonlinear registration algorithms can be found in [44]. In FreeSurfer [27] nonlinear intensity based registration using optical flow is a subroutine in one of the available registration algorithms [59].

We consider the image registration problem as an optimal control problem, which is governed by an optical flow, modelled by a hyperbolic transport equation, see [7]. Analysis of the transport equation in spaces with spatial BV regularity and optimal control formulations can, e.g., be found in [23, 2, 19, 18, 13, 37, 36]. A numerical implementation can, e.g., be found in [49, 50, 48, 10]. In recent years, image registration has been addressed via deep neural networks [29, 31, 14]. In order to contribute to closing the gap between classical approaches and neural networks based approaches, we consider a discretization of the optimal control formulation, which can be translated into a deep neural network architecture using convolutional neural networks, MeshGraphNet and ResNet architectures. This is inspired by [62], where neural network architectures are motivated by using an explicit time-stepping for time-dependent partial differential equations. Instead of only considering the partial differential equations, we design the algorithm in such a way that the whole control-to-state map is translatable into a neural network architecture. To do so, we base our algorithm on a discretization with Discontinuous Galerkin finite elements. The sketch of the implemented image registration algorithm is presented in Figure 2. Theoretical results show the limitations of our implementation. In this work, we implement the algorithm using classical discontinuous finite element techniques in order to do a proof-of-concept study.

We start by considering the relation between image registration and shape optimization in section 1.1. Both fields rely on finding an optimal transformation. To parametrize these transformations, similar ideas are present in the two fields. In this work, we are going to consider a method that is known as velocity or speed method in the shape optimization community and closely related to the large deformation diffeomorphic metric mapping (LDDMM) in image registration [70, 24, 4]. In shape optimization literature, the most general regularity requirements for the transformations is bi-Lipschitz continuity, i.e., functions that are Lipschitz continuous and have a Lipschitz continuous inverse. In section 2, we collect theoretical results, which show that this property is fulfilled if the velocity field defining the transformation is Lipschitz continuous. Moreover, the LDDMM approach can be related to a transport equation. Hence, the registration becomes a PDE constrained optimization problem (section 3). In section 4, we derive the DG upwinding scheme from the continuous weak form under

restrictive assumptions, which also indicate the theoretical limitations of the chosen approach. Section 5 presents the numerical implementation. Numerical results are given in section 6.

1.1. Relation between transformation based shape optimization and image registration. Though mainly being developed independently, image registration and transformation based shape optimization are based on similar techniques. In both applications, the goal is to find transformations, which ensure that the transformed meshes or images do not degenerate. In order to ensure this, several techniques have been developed and applied in the mathematical imaging as well as the shape optimization community. Overview over techniques in image registration can also be found in [77]. We also refer to [42].

Perturbation of Identity. One possibility to choose the transformation is a perturbation of identity ansatz

$$\tau = \text{id} + d_\tau,$$

where $d_\tau : \Omega \rightarrow \mathbb{R}^d$ denotes a deformation field. In order to obtain volume preservation, [30] worked with the constraint $\det(\nabla\tau) = 1$. According to [77], [39] modified this constraint to ensure $\det(\nabla\tau) > 0$. Working with transformations, which fulfill this property is also required for partial differential equations (PDE) constrained shape optimization, see [32, Lemma 2.3]. A result, which works only locally around the identity and does not use the determinant constraint can already be found in [76, Prop. 8.6]. In contrast to image registration, in shape optimization one is only interested in the shape of the domain, which is uniquely determined by its boundary. Hence, in order to have a one-to-one correspondence between shapes and transformations, in the method of mappings, see e.g. [54, 8, 26], the deformations are parameterized by scalar valued functions on the design boundary.

Velocity or speed method. Another possibility is the definition of the transformation τ via

$$\tau_\mathcal{V} := x_\mathcal{V}(1),$$

where $x_\mathcal{V}$ is the solution of

$$\begin{aligned} \partial_t x_\mathcal{V}(t) &= \mathcal{V}(t, x_\mathcal{V}(t)), \\ x_\mathcal{V}(0) &= x. \end{aligned}$$

Solution theory for this setting is available for $\mathcal{V} \in L^1((0, 1), \mathcal{C}^{0,1}(\overline{\mathbb{R}}, \mathbb{R}^d))$ [21, Sec. 4.2.1], see [79, 80]. In [76, Theorem 8.7], it is shown that for $\mathcal{V} \in L^1((0, 1), \mathcal{C}_0^1(\overline{\Omega}, \mathbb{R}^d))$ the transformation $\tau_\mathcal{V}$ is a diffeomorphism. In image registration, this choice for the transformation is known as LDDMM (Large deformation diffeomorphic metric mapping) algorithm [70, 24, 4]. Theoretical guarantees for $\tau_\mathcal{V}$ to be a diffeomorphism can be found in [76, Theorem 8.7].

2. On the properties of the transformations. In shape optimization, one is typically interested in transformations that are bi-Lipschitz, i.e., bijective and Lipschitz continuous with Lipschitz continuous inverse. If, e.g., a kink should appear after the optimization, a transformation is needed that is less regular than a \mathcal{C}^1 -diffeomorphism. The following lemma extends [76, Theorem 8.7] or [13] to this case, and is in the spirit of [12, Prop. 3.4] or [32, Lemma 2.2]. The lemma follows directly from [37, Theorem 5.1.8].

LEMMA 1. *Let $\Omega \subset \mathbb{R}^d$, $d \in \{2, 3\}$, be a bounded Lipschitz domain, $T > 0$ and let v be in $L^1((0, T), W^{1,\infty}(\Omega))$ with $v|_{\partial\Omega} = 0$. Moreover, for $t_0 \in (0, T)$, let X_{t_0} be defined as the solution of*

$$(1) \quad \begin{aligned} \partial_t X_{t_0}(x, t) &= v(X_{t_0}(x, t), t) && \text{on } \Omega \times (0, T), \\ X_{t_0}(x, t_0) &= x && \text{in } \Omega. \end{aligned}$$

Then, the transformation $\tau : \Omega \rightarrow \Omega$ defined by $\tau(x) = \tau_{t_0,s}(x) := X_{t_0}(x, s)$ is bi-Lipschitz continuous for all $s \in [0, T]$ and its inverse $\tau_{t_0,s}^{-1}(x) = X_s(x, t_0)$ satisfies

$$(2) \quad \begin{aligned} \partial_t X_s(x, t) &= v(X_s(x, t), t) && \text{on } \Omega \times (0, T), \\ X_s(x, s) &= x && \text{in } \Omega. \end{aligned}$$

Moreover, $X_{t_0}(x, s) = \eta(x, t_0, s)$, where η satisfies the transport equation

$$(3) \quad \begin{aligned} \partial_t \eta(x, t, s) + (v(x, t) \cdot \nabla) \eta(x, t, s) &= 0 && \text{on } \Omega \times (0, T), \\ \eta(x, s, s) &= x && \text{in } \Omega. \end{aligned}$$

Proof. Due to [37, Theorem 5.1.8 (i), (ii)] and [42, Lemma 2.1], $\tau_{t_0,t}$ is bijective and Lipschitz continuous. Due to [37, Theorem 5.1.8 (iv)], the inverse $\tau_{t_0,t}^{-1}$ is given as the solution of (2) and therefore also Lipschitz continuous. The latter follows from [37, Theorem 5.1.8 (v)]. \square

3. Problem formulation. We are concerned with finding a diffeomorphic mapping that transforms some input function ϕ_a to a target function ϕ_e . Let $\Omega \subset \mathbb{R}^d$, $d \in \{2, 3\}$, be a bounded Lipschitz domain, and $\phi_a, \phi_e, \phi(\cdot, T) : \Omega \rightarrow \mathbb{R}$ be scalar-valued. We consider the PDE constrained optimization problem

$$(4) \quad \min_{v \in V_{ad}} \frac{1}{2} \mathcal{J}(\phi(\cdot, T), \phi_e) + \gamma \mathcal{R}(v)$$

$$(5) \quad \begin{aligned} \text{s.t. } & \partial_t \phi(x, t) + v(x) \cdot \nabla \phi(x, t) = 0 & \text{on } \Omega \times (0, T) =: Q_T, \\ & \phi(\cdot, 0) = \phi_a & \text{in } \Omega, \end{aligned}$$

where $V_{ad} := \{v \in V : v \cdot n = 0 \text{ on } \Sigma_T := \partial\Omega \times (0, T)\}$ denotes the deformation velocity field, V denotes an appropriate Banach space, and $\gamma > 0$ a regularization parameter. The term $\mathcal{R}(v)$ denotes a regularization term, and the choice of regularization for the numerical results presented in manuscript are detailed in Section 5.2. We define the data mismatch as

$$(6) \quad \mathcal{J}(\phi(\cdot, T), \phi_e) = \int_{\Omega} f(\phi(x, T) - \phi_e(x)) dx.$$

For the choice of f , the square function has been considered in the image registration literature, e.g. [49]. To account for outliers in the image intensities, other functions are also used in brain image registration. Examples include the Huber function [35] and Tukey's biweight function [71] as used in, e.g., FreeSurfer [61], which both limit the influence of outliers in the loss and its gradient. Similar performance of these two choices in image registration has been observed in [3].

Here, we use the Huber function [35] defined as

$$(7) \quad f(x) = \begin{cases} \frac{x^2}{2} & \text{if } |x| \leq \delta, \\ \delta(|x| - \frac{\delta}{2}) & \text{otherwise,} \end{cases}$$

with $\delta > 0$.

In this manuscript, we are concerned with the registration of MR images. Hence, in our setting, $d = 3$ and $\Omega = [0, n_1 - 1] \times [0, n_2 - 1] \times [0, n_3 - 1]$ where n_i denote the numbers of voxels along image axis $i \in \{1, 2, 3\}$. $\phi_a, \phi_e, \phi(\cdot, T)$ correspond to intensity values in input, target and deformed input MRI, respectively.

4. Discrete setting. We use discontinuous Galerkin (DG) finite elements to discretize ϕ_e and ϕ_a . This seems to be a natural choice since the images are typically piecewise constant on voxels. Moreover, using a DG approach allows us to compute the inverse of the mass matrix element-wise, since the mass matrix attains a block-diagonal structure, where each block addresses the degrees of freedom of one cell. We first introduce some notation. Let the finite element mesh on $\Omega = \Omega_h$ be given as a collection of cells $E \in \mathcal{E}_h$ and interior facets $F \in \mathcal{F}_h$. Let $x \in F$ and denote by E_1, E_2 the neighboring cells of the facet F , chosen arbitrarily but fixed. We then define jumps and averages analogously to [22, Def. 1.17] as

$$\begin{aligned} \{\{v\}\}(x) &:= \frac{1}{2}(v|_{E_1}(x) + v|_{E_2}(x)), \\ \llbracket v \rrbracket(x) &:= v|_{E_1}(x) - v|_{E_2}(x). \end{aligned}$$

The outwards pointing normal vector on each element $E \in \mathcal{E}_h$ is denoted by n_E . Moreover, on the exterior domain boundary, the normal $n_F = n|_F$ is the outwards pointing normal vector. On interior facets, it is the normal vector pointing from $E_1(F)$ to $E_2(F)$, see [22, Fig. 1.4]. In the following, whenever we write E_1 or E_2 , we mean $E_1(F)$ and $E_2(F)$ depending on the facet F that we are considering. Moreover, let $V_h := \mathbb{P}_d^k(\mathcal{E}_h)$, where

$$(8) \quad \mathbb{P}_d^k(\mathcal{E}_h) := \{v \in L^2(\Omega) : \forall E \in \mathcal{E}_h, v|_E \in \mathbb{P}_d^k(E)\}$$

and $\mathbb{P}_d^k(E)$ denotes the space of polynomials of d variables with degree of at most k on E [22, Sec. 1.2.4].

We know that for sufficiently smooth v and ϕ_a the solution of (5) fulfills

- by definition the weak form

$$(9) \quad \int_0^T \int_{\Omega} \phi(x, s) (\partial_s \psi(x, s) + \operatorname{div}(\psi(x, s) v(x))) dx ds = - \int_{\Omega} \phi_a(x) \psi(x, 0) dx$$

for all $\psi \in \mathcal{C}_c^\infty([0, T] \times \Omega)$, see [36, Definition 2.1] or, for divergence free velocities, [13, Definition 2].

- the relation

$$(10) \quad \phi(x, t) = \phi_a(X(x, t)),$$

where X is the solution of

$$(11) \quad \begin{aligned} \partial_t X + \nabla X^\top v &= 0 && \text{on } Q_T, \\ X(0) &= x && \text{in } \Omega, \end{aligned}$$

see [13, Theorem 4] or, under mild regularity assumptions, [37, Theorem 5.1.15].

We show that the upwind DG scheme [22, (3.8)] can be derived from (9) and (10) if it is assumed that $\phi \in \mathcal{C}^1([0, T], V_h)$. This assumption is restrictive, since it implies that, for every t , $\phi(\cdot, t)$ can be exactly represented as a piecewise polynomial function on a temporally fixed discretization. This also implies that jumps are only allowed to appear at cell boundaries and are not allowed to move into the interior of the cells. In [22, Chapter 3], it is shown that for $\phi \in \mathcal{C}^0([0, T], H^1(\Omega)) \cap \mathcal{C}^1([0, T], L^2(\Omega))$ the scheme derived under the assumption $\phi \in L^1((0, T), V_h)$ combined with appropriate explicit time-stepping scheme converges towards the true solution for decreasing time step and mesh size as long as an appropriate CFL condition is fulfilled.

For solutions with jumps, the literature is scarce. The upwind scheme [22, (3.8)] can lead to spurious oscillations for higher order DG methods [22, Section 3.1.4.4]. In 1d, the regions around the shocks, so-called pollution regions, can be quantified [66, 78, 16]. In order to avoid oscillations, monotonicity preserving schemes were introduced. Godunov's theorem states that linear monotonicity preserving schemes can at most be first order accurate. Further research in that area, also in the context of non-linear hyperbolic equations, is devoted to circumvent Godunov's theorem, which led to MUSCL, TVD and other schemes. The topic is discussed in more detail in [47].

Motivated by the consideration in section 2, we consider velocity fields $v \in W^{1, \infty}(\Omega)^d$ such that $v|_{\Omega} = 0$ on the outer boundary of Ω . There is also literature on weaker regularity of v , see, e.g., [36]. Moreover, we assume that $\phi \in \mathcal{C}^1([0, T], V_h)$. Then we search for the solution in the space $\mathcal{C}^1((0, T), V_h)$, which also includes functions that are discontinuous along the facets. In order to derive the upwind DG scheme [22, (3.8)] under this restrictive assumption, we are going to take advantage of knowledge about the solution (Lemma 2).

We start with the weak form of the transport equation of (5)

$$\int_0^T \int_{\Omega} \phi(x, s) (\partial_s \psi(x, s) + \operatorname{div}(\psi(x, s) v(x))) dx ds = - \int_{\Omega} \phi_a(x) \psi(x, 0) dx$$

for all $\psi \in \mathcal{C}_c^\infty(\Omega \times [0, T])$. Note that s denotes the time variable here.

Integrating (4) by parts in space yields

$$(12) \quad \begin{aligned} & \int_0^T \int_{\Omega} \phi(x, s) \partial_s \psi(x, s) dx ds - \int_0^T \sum_{E \in \mathcal{E}_h} \int_E \psi(x, s) v(x) \cdot \nabla \phi(x, s) dx ds \\ & + \int_0^T \sum_{E \in \mathcal{E}_h} \int_{\partial E} \psi(x, s) \phi(x, s) v \cdot n_E dS ds = - \int_{\Omega} \phi_a(x) \psi(x, 0) dx. \end{aligned}$$

Collecting the integrals over the boundaries of the elements as integrals over facets yields

$$(13) \quad \begin{aligned} & \int_0^T \int_{\Omega} \phi(x, s) \partial_s \psi(x, s) dx ds - \int_0^T \sum_{E \in \mathcal{E}_h} \int_E \psi(x, s) v(x) \cdot \nabla \phi(x, s) dx ds \\ & + \int_0^T \sum_{F \in \mathcal{F}_h} \int_F \psi(x, s) [\phi(x, s)] v \cdot n_F dS ds = - \int_{\Omega} \phi_a(x) \psi(x, 0) dx, \end{aligned}$$

Since, in (13), there is no derivative on ψ left, we can leverage the requirements on ψ by considering (13) for a sequence of smooth functions ψ_n that we pass to the limit. Choosing ψ_n such that $\lim_{n \rightarrow \infty} \|\psi_n - 1_E\|_{L^p(\Omega)} = 0$ for some $p \in [1, \infty)$ and 1_E denoting the characteristic function of E , and summing up over the elements yields

$$(14) \quad \int_0^T \int_{\Omega} \phi(x, s) \partial_s \psi(x, s) dx ds - \int_0^T \sum_{E \in \mathcal{E}_h} \int_E \psi(x, s) v(x) \cdot \nabla \phi(x, s) dx ds = - \int_{\Omega} \phi_a(x) \psi(x, 0) dx$$

for all $\psi \in \mathcal{C}_c([0, T), V_h)$.

With the same argumentation, but a sequence of smooth ψ_n that converges to 1 on the facets and 0 in the interior of the elements, we obtain

$$(15) \quad \int_0^T \sum_{F \in \mathcal{F}_h} \int_F \psi_F(x, s) [\phi(x, s)] v \cdot n_F dS ds = 0$$

for all $\psi_F \in \mathcal{C}_c^\infty([0, T), C(\bar{F}))$ and $F \in \mathcal{F}$.

Integrating (14) by parts yields

$$(16) \quad \begin{aligned} & \int_0^T \int_{\Omega} \phi(x, s) \partial_s \psi(x, s) dx ds + \int_0^T \sum_{E \in \mathcal{E}_h} \int_E \operatorname{div}(\psi(x, s) v(x)) \phi(x, s) dx ds \\ & - \int_0^T \sum_{F \in \mathcal{F}_h} \int_F [\psi(x, s) \phi(x, s)] v \cdot n_F dS ds = - \int_{\Omega} \phi_a(x) \psi(x, 0) dx, \end{aligned}$$

which is equivalent to

$$(17) \quad \begin{aligned} & \int_0^T \int_{\Omega} \phi(x, s) \partial_s \psi(x, s) dx ds + \int_0^T \sum_{E \in \mathcal{E}_h} \int_E \operatorname{div}(v(x)) \psi(x, s) \phi(x, s) dx ds \\ & + \int_0^T \sum_{E \in \mathcal{E}_h} \int_E \phi(x, s) v(x) \cdot \nabla \psi(x, s) dx ds - \int_0^T \sum_{F \in \mathcal{F}_h} \int_F [\psi(x, s) \phi(x, s)] v \cdot n_F dS ds \\ & = - \int_{\Omega} \phi_a(x) \psi(x, 0) dx. \end{aligned}$$

Let $t \in [0, T)$, $\Delta t > 0$ be such that $t + \Delta t \in (0, T]$. We consider a test function $\psi_{t, \Delta t}(x, s) = \psi(x) \chi_{t, \Delta t}(s)$ with a time-independent ψ and $\chi_{t, \Delta t}(s) = \begin{cases} 1 & \text{for } s \in (t, t + \Delta t), \\ 0 & \text{else.} \end{cases}$

Hence, (17) tested with $\psi_{t, \Delta t}$, is given by

$$(18) \quad \begin{aligned} & - \int_{\Omega} (\phi(x, t + \Delta t) - \phi(x, t)) \psi(x) dx + \int_t^{t + \Delta t} \sum_{E \in \mathcal{E}_h} \int_E \operatorname{div}(v(x)) \psi(x) \phi(x, s) dx ds \\ & + \int_t^{t + \Delta t} \sum_{E \in \mathcal{E}_h} \int_E \phi(x, s) v(x) \cdot \nabla \psi(x) dx ds - \int_t^{t + \Delta t} \sum_{F \in \mathcal{F}_h} \int_F [\psi(x) \phi(x, s)] v \cdot n_F dS ds = 0, \end{aligned}$$

if $t > 0$, and

$$(19) \quad \begin{aligned} & - \int_{\Omega} (\phi(x, t + \Delta t)) \psi(x) dx + \int_t^{t + \Delta t} \sum_{E \in \mathcal{E}_h} \int_E \operatorname{div}(v(x)) \psi(x) \phi(x, s) dx ds \\ & + \int_t^{t + \Delta t} \sum_{E \in \mathcal{E}_h} \int_E \phi(x, s) v(x) \cdot \nabla \psi(x) dx ds - \int_t^{t + \Delta t} \sum_{F \in \mathcal{F}_h} \int_F [\psi(x) \phi(x, s)] v \cdot n_F dS ds \\ & = - \int_{\Omega} \phi_a(x) \psi(x) dx, \end{aligned}$$

if $t = 0$. For the latter, considering $\Delta t \rightarrow 0$ yields the initial condition

$$(20) \quad \int_{\Omega} \phi(x, 0) \psi(x) dx = \int \phi_a(x) \psi(x) dx.$$

For the consideration of (18), we define

$$\begin{aligned}
f(\phi|_{E_1}, \phi|_{E_2}, v, n_F)(x, s) &:= \begin{cases} \phi|_{E_1}(x, s)v(x) \cdot n_F(x) & \text{if } v \cdot n_F \geq 0, \\ \phi|_{E_2}(x, s)v(x) \cdot n_F(x) & \text{else,} \end{cases} \\
&= \phi|_{E_1}(x, s) \max(0, v(x) \cdot n_F(x)) + \phi|_{E_2}(x, s) \min(0, v(x) \cdot n_F(x)) \\
&= \phi|_{E_1}(x, s) \max(0, v(x) \cdot n_F(x)) - \phi|_{E_2}(x, s) \max(0, v(x) \cdot (-n_F)(x)).
\end{aligned}$$

LEMMA 2. Let $t \in (0, T)$, $\phi(t), \psi \in V_h$ and X be defined as the solution of (11)

$$\begin{aligned}
\partial_t X + \nabla X^\top v &= 0 \quad \text{on } Q_T, \\
X(0) &= x \quad \text{in } \Omega.
\end{aligned}$$

Moreover, assume that (10) holds, i.e., ϕ is transported along the characteristics of X such that $\phi(x, s) = \phi(X(x, t - s), t)$. Then it holds

$$\begin{aligned}
(21) \quad &\lim_{\Delta t \rightarrow 0^+} \frac{1}{\Delta t} \int_t^{t+\Delta t} \int_F [\psi(x) \phi(x, s)] v \cdot n_F dS ds \\
&= \int_F [\psi(x)] f(\phi|_{E_1}(x, t), \phi|_{E_2}(x, t), v(x), n_F(x)) dS
\end{aligned}$$

for all $F \in \mathcal{F}_h$.

Proof. It holds that

$$\lim_{s \rightarrow t^+} \phi(X(x, t - s), t) v \cdot n_F = f(\phi|_{E_1}(x, t), \phi|_{E_2}(x, t), v(x), n_F(x)).$$

Hence, with the dominated convergence theorem,

$$\begin{aligned}
&\lim_{\Delta t \rightarrow 0^+} \frac{1}{\Delta t} \int_t^{t+\Delta t} \int_F [\psi(x) \phi(x, s)] v \cdot n_F dS ds \\
&= \lim_{\Delta t \rightarrow 0^+} \int_0^1 \int_F [\psi(x) \phi(x, t + \tilde{s}\Delta t)] v \cdot n_F dS d\tilde{s} \\
&= \int_F [\psi(x)] f(\phi|_{E_1}(x, t), \phi|_{E_2}(x, t), v(x), n_F(x)) dS.
\end{aligned}$$

□

LEMMA 3. Let $\phi \in \mathcal{C}^1([0, T], V_h)$ and $\psi \in L^1((0, T), V_h)$. Then it holds

$$(22) \quad \lim_{\Delta t \rightarrow 0^+} \frac{1}{\Delta t} \int_\Omega (\phi(x, t + \Delta t) - \phi(x, t)) \psi(x) dx = \int_\Omega \phi_t(x, t) \psi(x) dx,$$

and

$$(23) \quad \lim_{\Delta t \rightarrow 0^+} \frac{1}{\Delta t} \int_t^{t+\Delta t} \int_E \operatorname{div}(v(x)) \psi(x) \phi(x, s) dx ds = \int_E \operatorname{div}(v(x)) \psi(x) \phi(x, t) dx,$$

$$(24) \quad \lim_{\Delta t \rightarrow 0^+} \frac{1}{\Delta t} \int_t^{t+\Delta t} \int_E \phi(x, s) v(x) \cdot \nabla \psi(x) dx ds = \int_E \phi(x, t) v(x) \cdot \nabla \psi(x) dx,$$

for all $E \in \mathcal{E}_h$.

Proof. (22) follows from the dominated convergence theorem and the regularity of ϕ . To prove (23) we consider

$$\begin{aligned}
&| \frac{1}{\Delta t} \int_t^{t+\Delta t} \int_E \operatorname{div}(v(x)) \psi(x) \phi(x, s) dx ds - \int_E \operatorname{div}(v(x)) \psi(x) \phi(x, t) dx | \\
&= \frac{1}{\Delta t} | \int_t^{t+\Delta t} \int_E \operatorname{div}(v(x)) \psi(x) (\phi(x, s) - \phi(x, t)) dx ds | \\
&\leq \| \operatorname{div}(v(x)) \psi(x) \|_{L^\infty(E)} \max_{s \in [t, t + \Delta t]} \| \phi(x, s) - \phi(x, t) \|_{L^1(E)}
\end{aligned}$$

and use continuity of ϕ to show that the right hand side converges to zero for $\Delta t \rightarrow 0$. (24) follows analogously. □

Dividing (18) by Δt and considering the limit $\Delta t \rightarrow 0^+$ yields with Lemma 2 and Lemma 3:

$$(25) \quad \begin{aligned} & \int_{\Omega} \partial_t \phi(x, t) \psi(x) dx - \sum_{E \in \mathcal{E}_h} \int_E \operatorname{div}(v(x)) \psi(x) \phi(x, t) dx - \sum_{E \in \mathcal{E}_h} \int_E \phi(x, t) v(x) \cdot \nabla \psi(x) dx \\ & + \sum_{F \in \mathcal{F}_h} \int_F [\![\psi(x)]\!] f(\phi|_{E_1}(x, t), \phi|_{E_2}(x, t), v(x), n_F(x)) dS = 0. \end{aligned}$$

We set (25) in relation to the considerations in [22]. Doing another integration by parts for the $\int_E \phi(x, t) v(x) \cdot \nabla \psi(x) dx$ for all $E \in \mathcal{E}_h$ shows that (25) is equivalent to [22, (3.7)]. For the sake of clarity, we skip the dependencies on x and t and write \cdot_i instead of $\cdot|_{E_i}$, $i \in \{1, 2\}$. We obtain with integration by parts

$$- \int_E \phi v \cdot \nabla \psi dx = - \int_E \operatorname{div}(\phi \psi v) dx + \int_E \operatorname{div}(\phi v) \psi dx$$

and hence

$$(26) \quad \begin{aligned} & - \sum_{E \in \mathcal{E}_h} \int_E \phi v \cdot \nabla \psi dx = - \sum_{F \in \mathcal{F}_h} \int_F [\![\phi \psi]\!] v \cdot n_F dS \\ & + \sum_{E \in \mathcal{E}_h} \int_E \operatorname{div}(v) \phi \psi dx + \sum_{E \in \mathcal{E}_h} \int_E \psi v \cdot \nabla \phi dx. \end{aligned}$$

We know that

$$(27) \quad - \int_F [\![\phi \psi]\!] v \cdot n_F dS = - \int_F (\phi_1 \psi_1 - \phi_2 \psi_2) v \cdot n_F dS.$$

Moreover, we obtain

$$(28) \quad \int_F [\![\psi]\!] f(\phi_1, \phi_2, v, n_F) dS = \int_F [\![\psi]\!] \frac{1}{2} ((v \cdot n + |v \cdot n|) \phi_1 + (v \cdot n - |v \cdot n|) \phi_2) dS.$$

Summing up (27) and (28) yields

$$(29) \quad - \int_F [\![\phi \psi]\!] v \cdot n_F dS + \int_F [\![\psi]\!] f(\phi_1, \phi_2, v, n_F) dS = \int_F \frac{1}{2} |v \cdot n| [\![\phi]\!] [\![\psi]\!] dS - \int_F (v \cdot n) [\![\phi]\!] \{[\psi]\} dS.$$

Combining (25), (26) and (29) yields [22, (3.7)]. Hence, we are in the setting of [22, Chapter 3]. The convergence theory presented in [22] proves that convergence towards a true smooth solution can be ensured under a CFL condition $\Delta t \leq C \frac{h}{\|v\|_{L^\infty(\Omega)^d}}$ if one chooses a DG0-discretization in space combined with explicit Euler in time [22, Theorem 3.7] or a DG1-discretization in space combined with an explicit RK2 scheme in time [22, Theorem 3.10]. Moreover, it suggests that a more restrictive CFL condition is needed for DG1-discretization in space combined with explicit Euler in time [22, Remark 3.21].

5. Numerical realization. As discussed in the previous section, from a theoretical point of view, the input and target images ϕ_a and ϕ_e need to be either considered as discrete representations of smooth functions or preprocessed by smoothing in order to have theoretical guarantees for (25). In this work, we do the former. Nevertheless, a pre-processing step is involved in the algorithm, which is described in section 6.1.

5.1. Transport Equation. The discretized weak form (25) can be solved numerically using a second order Runge-Kutta method in time to deform the input image ϕ_a given some velocity field v . However, we want to use gradient-based optimization techniques to determine the unknown velocity v that deforms ϕ_a to a target ϕ_e . The discrepancy measure \mathcal{J}_d (4) needs to be differentiable with respect to v . This requires differentiability of the solution to (25) with respect to v . However, this is in general not the case. Due to the max operator, the upwind flux function in the (25) is not differentiable w.r.t. v in all points x , for which $v(x) \cdot n(x) = 0$. Therefore, we introduce a smoothed maximum operator defined as

$$\max_\epsilon(0, x) := \sigma_\epsilon(x) x$$

with

$$\sigma_\epsilon(x) = \frac{1}{1 + e^{-\frac{1}{\epsilon}x}}$$

and propose a smoothed version of the upwind scheme by using

$$(30) \quad f_\epsilon(\phi|_{E_1}, \phi|_{E_2}, v, n_F) := \phi|_{E_1} \max_\epsilon(0, v \cdot n_F) - \phi|_{E_2} \max_\epsilon(0, v \cdot (-n_F)).$$

This flux function is consistent since

$$\begin{aligned} f_\epsilon(\bar{\phi}, \bar{\phi}, v, n_F) &= \bar{\phi} \max_\epsilon(0, v \cdot n_F) - \bar{\phi} \max_\epsilon(0, v \cdot (-n_F)) \\ &= \bar{\phi}[\sigma_\epsilon(v \cdot n_F)v \cdot n_F - \sigma_\epsilon(v \cdot (-n_F))v \cdot (-n_F)] \\ &= \bar{\phi}[\sigma_\epsilon(v \cdot n_F) + \sigma_\epsilon(-v \cdot n_F)]v \cdot n_F \\ &= \bar{\phi}v \cdot n_F, \end{aligned}$$

where we used that the sigmoid function satisfies $\sigma_\epsilon(x) + \sigma_\epsilon(-x) = 1$.

We implement (25) with the smoothed flux term (30) in FEniCS [1] using a second order Runge-Kutta scheme in time. For the results reported in this manuscript, we use fixed $N = 100$ time steps and a time horizon $T = 1$. We discretize v using continuous linear Lagrange elements. The initial condition ϕ_0^h and the state ϕ are discretized by a discontinuous Galerkin method using first order polynomials.

We introduce the mapping from the initial condition to the final state via solving (5) as

$$(31) \quad \Phi_v : \phi_0^h \mapsto \phi^h(T),$$

where the subscript v indicates the dependence on the deformation velocity field.

5.2. Optimization. We want to find a velocity field based mapping, such that a discrepancy measure \mathcal{J}_d between the deformed MRI of ‘‘Abby’’ and the MRI of ‘‘Ernie’’ becomes small. Due to the considerations in Lemma 1, the velocity needs to be smooth enough; more precisely, in $W^{1,\infty}(\Omega)$. Optimization in $W^{1,\infty}(\Omega)$ is challenging and subject to current research in the context of shape optimization [20]. We consider an alternative approach that works in a Hilbert space setting, i.e., optimization for $v \in H^2(\Omega)$. This is justified from a discretized perspective, since discretization with CG1 finite elements combined with the discretized H^k -norm, $k \geq 1$, ensures the regularity requirements of Lemma 1 if the mesh is fixed. In order to avoid a discretization of the velocity v with H^2 -conforming finite elements, we introduce an auxiliary variable $\tilde{v} \in L^2(\Omega)$ from which v is computed via solving the elliptic problem

$$(32) \quad \begin{aligned} \alpha v - \beta \Delta v &= \tilde{v} && \text{in } \Omega, \\ v &= 0 && \text{on } \partial\Omega. \end{aligned}$$

Here, $\alpha, \beta > 0$ are hyperparameters and their influence will be discussed in the numerical results in Section 6. We hence optimize \mathcal{J}_d for $\tilde{v} \in L^2(\Omega)$. General-purpose optimization algorithms, such as L-BFGS-B [46] implemented in SciPy [75], work with the Euclidean inner product ℓ^2 . Directly using the nodal values \tilde{v}_i of \tilde{v} as ℓ^2 control variable can lead to slow convergence [64, 40]. We use bold-face symbols to denote the degrees of freedom of the corresponding finite element function. We hence introduce the control variable $\hat{v} \in \mathbb{R}^n$ where n is the number of degrees of freedom of the finite element discretization of \tilde{v} . The former are related via the linear transformation

$$(33) \quad \hat{v} = \mathcal{C}^{-1} \hat{v},$$

where $\mathcal{C}^\top \mathcal{C} = \mathcal{M}$ is the Cholesky factorization of the inner product matrix \mathcal{M} . In our case, \mathcal{M} is the lumped mass matrix and hence the linear transformation (33) is a scaling and promotes mesh independence.

We note that directly working with control variables $v \in H^1(\Omega)$ and applying the linear transformation requires computing the action of the inverse of the Cholesky factors of the stiffness matrix. This is not currently implemented in parallel in our software framework, and therefore we use the approach presented above. A graphical summary of the approach is given in Fig. 2.

We work with the regularization (4) defined by

$$(34) \quad \mathcal{R}(v) = \mathcal{R}(v(\tilde{v})) = \int_{\Omega} \tilde{v}^2 dx.$$

Alternatively, one could also directly work with $\hat{\mathbf{v}} \cdot \hat{\mathbf{v}}$.

We use the pre-registered MRI from “Abby” as initial condition $\phi(\cdot, 0)$ and the starting guess $\hat{\mathbf{v}} = 0$ to solve (5) numerically using the proposed discretization implemented in FEniCS [1] as described in Section 5.1. Gradients of the cost functional with respect to the control \hat{v} are obtained using the dolfin-adjoint software [25].

To allow for more complex deformations, we take a multi-step approach. In detail, we start with the affine registered image from “Abby” and optimize for the first velocity field $v = v_1$ with a fixed number of iterations of L-BFGS-B. Starting from the resulting deformed image, we optimize for a new deformation velocity field v_2 . This scheme is applied for a fixed number of times.

The final transformation of the input image to target image is then given as

$$(35) \quad \mathcal{F} = \Phi \circ \mathcal{A} = \Phi_N \circ \dots \circ \Phi_1 \circ \mathcal{A},$$

where we shortly write Φ_i for deformations via distinct velocity fields $v = v_i$.

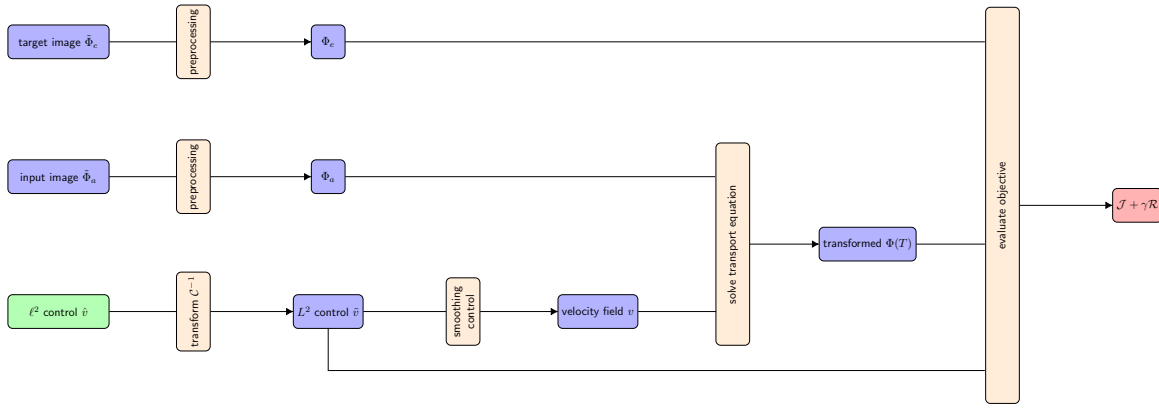


FIGURE 2. Implementation of the velocity-based image registration Φ .

5.3. Mesh transformation pipeline. In the following, we describe how the vertex coordinates of the input mesh from “Abby” are deformed to obtain a new mesh for “Ernie”. We use SVMTK [73] as described in [52] to create the reference mesh for “Abby”. The meshing pipeline in SVMTK uses the surface files generated by the FreeSurfer recon-all command, which automatically generates cortical surface meshes and brain segmentations from MRI. For the numerical results presented in this paper, we assume that recon-all has been run successfully on subject a , and use the automatic parcellation output file `aseg.mgz` as well as the left pial surface (the left hemisphere brain surface) file `lh.pial` this command generates. We distinguish between $\mathbf{x} \in \mathbb{R}^3$ for the coordinate of a vertex on a FreeSurfer surface and the corresponding coordinate $\mathbf{a} \in [0, 256]^3$ in the MR voxel space as

$$(36) \quad \mathbf{a} = \mathcal{R}_a \mathbf{x}.$$

Here, $\mathcal{R}_a \in \mathbb{R}^{4 \times 4}$ is the affine transform between coordinates defined in FreeSurfer-tkr space and voxel space, cf., e.g., [52, Section 4.4] for details on the coordinate systems involved in the mesh generation. The subscript a indicates that this subject transformation is subject-specific.

In (35) we defined \mathcal{F} as the mapping that registers the input image to the target, i.e.,

$$(37) \quad \phi(\cdot, T)(\mathbf{a}) = \phi_a(\mathbf{e}) \quad \text{with} \quad \mathbf{e} = \mathcal{F}^{-1} \mathbf{a}$$

Where the action of the transformation on the (voxel) coordinates is understood to be component-wise,

$$(38) \quad e_i = \mathcal{F}^{-1} a_i, \quad i \in \{1, 2, 3\}.$$

The inverse of \mathcal{F} is

$$(39) \quad \mathcal{A}^{-1} \circ \Phi_1^{-1} \circ \dots \circ \Phi_N^{-1}.$$

Finally, in order to compare the meshes generated by our approach to surfaces generated by FreeSurfer recon-all, we transform the deformed mesh coordinates \mathbf{e} into the FreeSurfer surface coordinate space by

$$(40) \quad \mathbf{y} = \mathcal{R}_e^{-1} \mathbf{e}.$$

6. Numerical experiments. We apply the method to register the brain MRI scan of two human subjects taken from [52]. Using the software provided in [52], we create two template meshes from the MRI of “Abby”: one for the ventricular system, including the cerebral aqueduct, as well as a mesh for the left hemisphere. Our primary goal here is to use the image registration transformation to deform the mesh matching the template subject “Abby” to match the anatomy of “Ernie”.

6.1. Image pre-processing. We first apply several pre-processing steps to the MR images to reduce the computational cost associated with our algorithm. We use the output images `brain.mgz` displaying only the brain with the cranium and other soft tissue of the head removed for both subjects, which is again achieved via the recon-all command of FreeSurfer. This is beneficial since it allows us to exclude slices on the boundaries of the MRI that do not contain brain tissue, significantly reducing the computational cost of the algorithm. Coronal slices of these images for both subjects are shown in Fig. 1.

Next, a pre-registration step using an affine transformation \mathcal{A} (12 degrees of freedom) [61] is performed. Then the MR image intensities are normalized as proposed in [55, 56] and implemented in [60]. While many normalization schemes have been proposed in the literature, e.g., [28, 68, 15], the results in the study [65] suggest efficacy of the approach [55, 56] and we hence resort to this normalization.

Finally, to reduce the computational cost of the nonlinear registration, we cut the images to the rectangular bounding box containing both images, but pad the image with 2 voxels containing zeros on every side (due to Dirichlet boundary condition $v = 0$ for the deformation velocity). This reduces the number of voxels from $256^3 \approx 1.7 \times 10^7$ in the original images to $n_1 \times n_2 \times n_3 = 147 \times 154 \times 192 \approx 4.4 \times 10^6$ whilst keeping the full brain in the image.

The cropped image intensities are then represented as a discontinuous finite element function using first order Lagrange elements defined on a Box Mesh with $6 \times n_1 \times n_2 \times n_3$ cells and length scales $n_1 \times n_2 \times n_3$.

6.2. Results. We present results obtained with a series of four velocity field registrations $\Phi_4, \Phi_3, \Phi_2, \Phi_1$ with distinct velocity fields v_4, v_3, v_2, v_1 . That is, the intermediate deformed images ϕ_1, ϕ_2, ϕ_3 and the final deformed image $\phi = \phi_4$ are created by restarting the algorithm on the previous results, i.e.,

$$(41) \quad \phi_1 = (\Phi_1 \circ \mathcal{A})\phi_a, \quad \phi_2 = \Phi_2\phi_1, \quad \phi_3 = \Phi_3\phi_2, \quad \phi = \Phi_4\phi_3.$$

Recall that ϕ_a denotes the preprocessed template image from “Abby” and the target image from “Ernie” is denoted by the symbol ϕ_e .

In the remainder of this section we first discuss the quality of the image registration in Subsection 6.2.1, and in Subsection 6.2.2 we discuss the application of the deformations to two different template meshes. The results after three and four deformations are discussed separately in each subsection to elaborate on the influence of the hyperparameters α, β in the velocity smoothing (32).

6.2.1. Image registration. We first optimize a series of three velocity registrations Φ_3, Φ_2, Φ_1 with distinct velocity fields v_3, v_2, v_1 for a total of 400 iterations of L-BFGS-B. The hyperparameters to smoothen the control are set to $\alpha = 0, \beta = 1$. In detail, we start from the affine registered image $\mathcal{A}\phi_a$ and optimize v_1 such that the discrepancy between the deformed image ϕ_1 and the target image ϕ_e is reduced. We then hold v_1 fixed and optimize v_2 such that the discrepancy between $\phi_2 = \Phi_2\phi_1$ and ϕ_e is further reduced, and do the same for Φ_3 applied to ϕ_2 . This procedure reduces the L^2 -discrepancy between deformed image and target by 60 % (relative to the affine pre-registration), cf. Fig. 3.

In the left panel in Fig. 4 we show the absolute difference between deformed image ϕ_3 and target in color (heatmap) together with the target MRI (greyscale) in an exemplary axial slice. From the

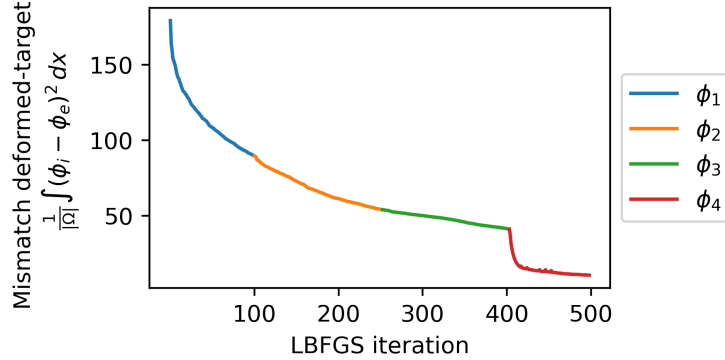


FIGURE 3. Reduction of the L^2 -norm between deformed image and target during optimization of the velocity field deformations Φ_i , $i = 1, 2, 3, 4$, with the L-BFGS-B algorithm. ϕ_1, ϕ_2, ϕ_3 are obtained with $\alpha = 0, \beta = 1$ and ϕ_4 is obtained with $\alpha = 0.5, \beta = 0.5$.

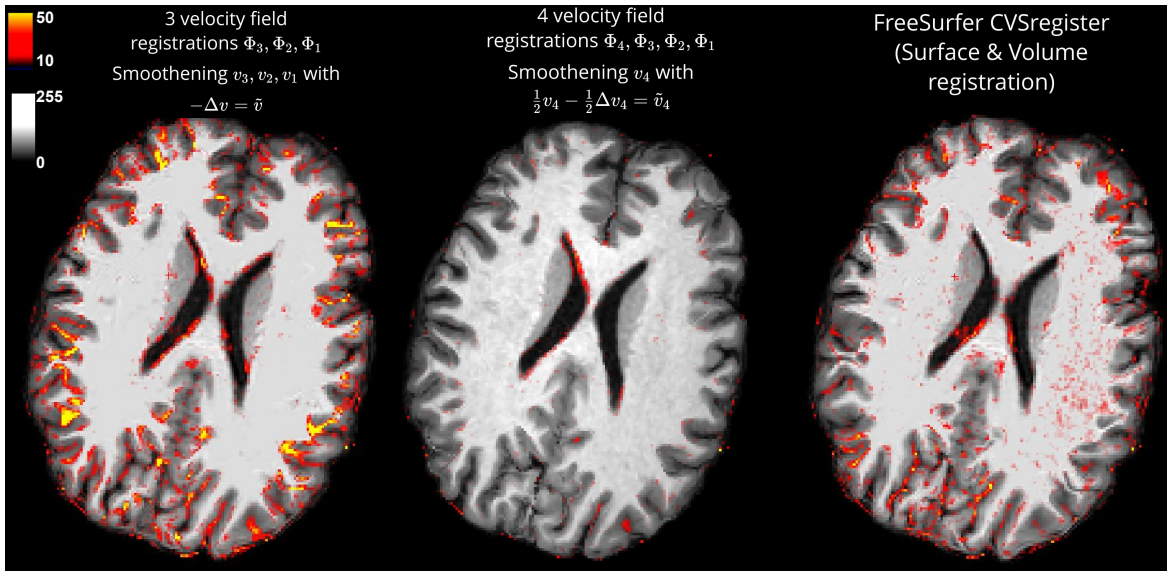


FIGURE 4. Background MR images: Slices from target image “Ernie” ϕ_e . The heatmap show the absolute difference $|\phi_e - \phi|$ between target ϕ_e and images registered with different procedures. Left: Affine and three velocity field deformations $\Phi_3 \circ \Phi_2 \circ \Phi_1 \circ \mathcal{A}$ with $\alpha = 0, \beta = 1$. Center: Affine and four velocity field deformations $\Phi_4 \circ \Phi_3 \circ \Phi_2 \circ \Phi_1 \circ \mathcal{A}$ with $\alpha = 1, \beta = 0.1$ for Φ_4 . Right: FreeSurfer cvs-register [59].

figure we observe that the remaining error is largely due to mismatch between the cortical folding patterns of the registered and the target image. The ventricles (the two large black space in the center of the brain), however, are registered fairly well (low mismatch around the ventricles as indicated by the color in Fig. 4).

We next investigate whether our approach can improve upon the registration by changing the parameters α, β in (32). We apply a fourth registration Φ_4 with velocity field v_4 to the deformed image ϕ_3 obtained with the procedure described above. For this velocity field, we change from $\alpha = 0, \beta = 1$ to $\alpha = \beta = 1/2$. As can be seen from Fig. 3, the mismatch between deformed image and target can be further reduced from 40 % to 20 % (relative to the affine pre-registration) after optimizing v_4 for 100 iterations. The registered image matches visually well with the target. In fact, in the exemplary slice shown in Fig. 4, only some minor error is left close to the ventricle. The figure also shows the registration error obtained with the nonlinear registration provided by FreeSurfer cvs-register [59] (Surface and Volume based registration). The slice shown in Fig. 4 suggests that our algorithm yields registration with favourable accuracy compared to the FreeSurfer algorithm.

6.2.2. Mesh registration. Using the registration deformation obtained above, we test the deformation of two different meshes, one for the ventricular system and one for the left hemisphere. The

ventricular system is chosen because this is an example, where manual mesh processing is required and we want to demonstrate that our registration can be used to create a new ventricular system mesh for the target without manual corrections. The left hemisphere mesh is chosen to show the limitations of our algorithm in the current formulation.

We create a ventricular system mesh for the template “Abby” by utilizing the automatic segmentation image `aseg.mgz` provided by FreeSurfer and mark the cerebral aqueduct manually (cf. Fig. 5A). Using the processing steps described in [52], we create a volume mesh for the ventricular system (cf. Fig. 5C). The mesh for the left hemisphere is generated using the post-processing steps in [52] from the surface `lh.pial` generated by FreeSurfer’s `recon-all` command.

First, we apply the transformations \mathcal{A} (affine pre-registration), $\Phi_1 \circ \mathcal{A}$ (affine and one velocity field deformation) as well as $\Phi_3 \circ \Phi_2 \circ \Phi_1 \circ \mathcal{A}$ (affine and three velocity field deformations) to the ventricular system mesh and compare the boundaries of these meshes in Fig. 6. It can be seen that the affine registered mesh does not match the target “Ernie” at all (red contours in Fig. 6). Transport with one velocity field gives visibly better agreement (orange contours in Fig. 6). To resolve finer details and obtain meshes that are accurate to within a few voxels, two more velocity fields are needed (green contours and blue arrows in Fig. 6).

Figure 5D shows the deformed mesh. It can be seen that the mesh transformation with $\Phi_3 \circ \Phi_2 \circ \Phi_1 \circ \mathcal{A}$ yields a mesh with similar smooth surface as the input mesh. Hence, one does not need to manually label the cerebral aqueduct, which is missing in the FreeSurfer automatic segmentation of “Ernie” (Fig. 5B).

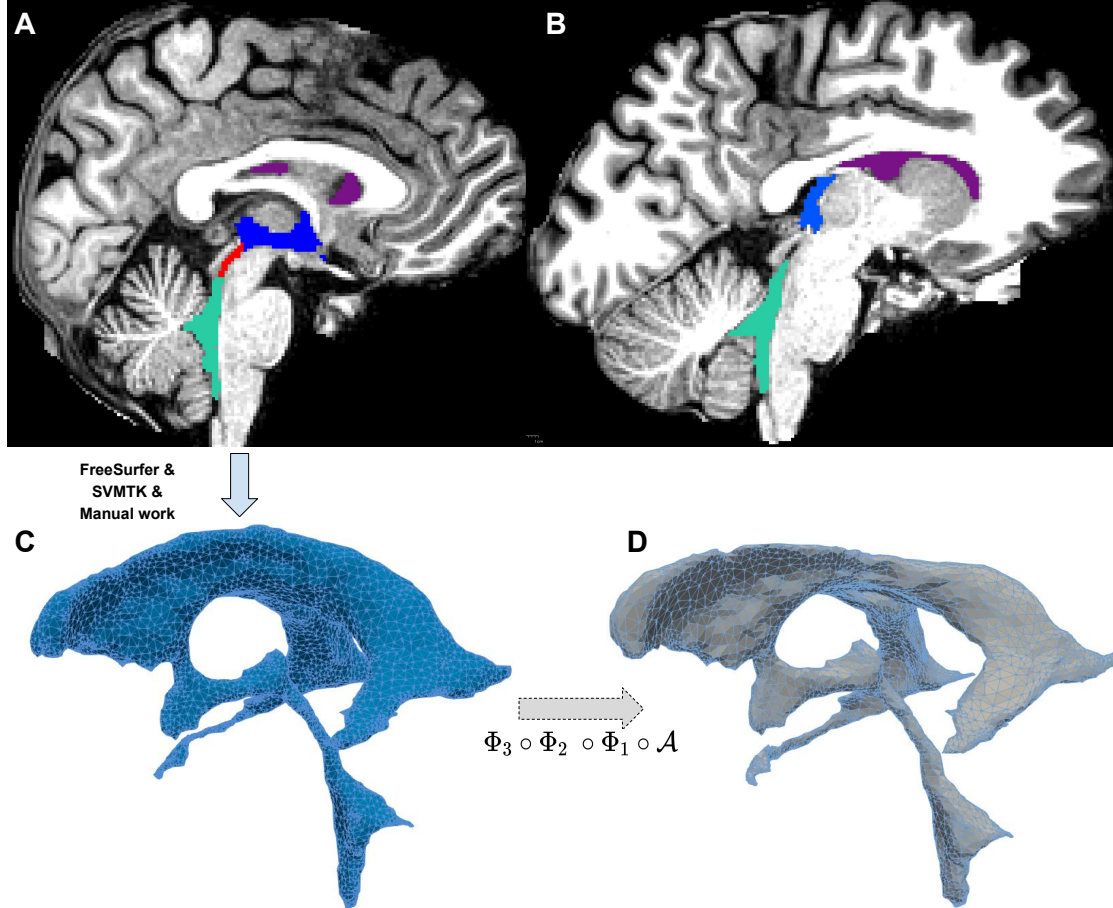


FIGURE 5. A-B: Sagittal slice of “Abby” and “Ernie” with the FreeSurfer automatic segmentation for fourth ventricle (cyan), third ventricle (blue) and lateral ventricles (violet). After manually marking the cerebral aqueduct in “Abby” (displayed in red in A), we generate a mesh for the ventricular system of “Abby” (C). The same nonlinear registration $\Phi_3 \circ \Phi_2 \circ \Phi_1 \circ \mathcal{A}$ that registers the MR image of “Abby” to “Ernie” can be used to obtain a mesh for the ventricular system of “Ernie” (D).

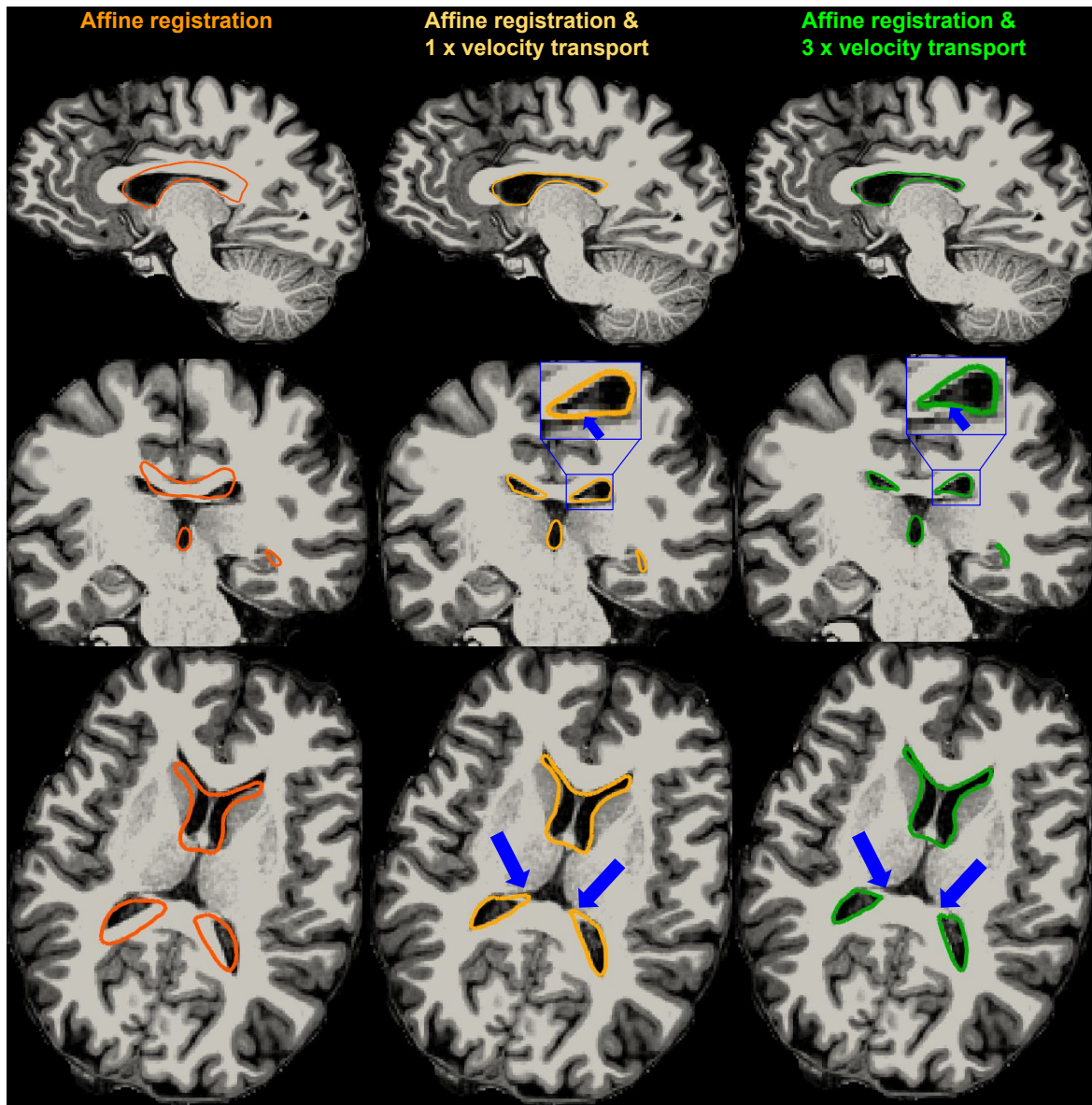


FIGURE 6. *Background MR images: Slices from target image “Ernie”. Colored lines: surfaces of deformed ventricle mesh from input “Abby”. Orange: Mesh deformed with affine deformation \mathcal{A} , Yellow: Affine and one velocity field deformation $\Phi_1 \circ \mathcal{A}$, Green: Affine and three velocity field deformations $\Phi_3 \circ \Phi_2 \circ \Phi_1 \circ \mathcal{A}$.*

We also test the application of all four velocity field registrations ($\Phi_4 \circ \Phi_3 \circ \Phi_2 \circ \Phi_1 \circ \mathcal{A}$) to the ventricular system mesh. A slice of the surface of the resulting deformed mesh is shown in blue in Fig. 7. It can be seen that the additional deformation does not improve upon the match to the ventricle. This was to be expected, since Fig. 4 shows that three velocity field deformations already register the ventricular system well to the target image. However, it can be seen that the quality of the deformed mesh decreases in the sense that the mesh surface becomes jagged. This is due to the fact that Φ_4 was obtained with $\alpha = \beta = 1/2$. The velocity pre-processing step (32) hence yields a velocity field with finer features than in Φ_3, Φ_2, Φ_1 obtained with $\alpha = 0, \beta = 1$. To mitigate this issue, a post-processing step (smoothing and isotropic remeshing as described in [52]) can be applied to the mesh surface. This yields a mesh very similar to the mesh obtained with three velocity fields shown in green in Fig. 4 (post-processed mesh not shown).

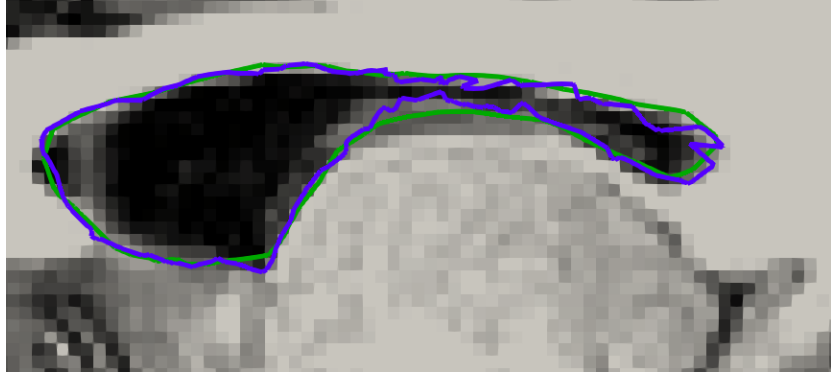


FIGURE 7. Surface of the deformed mesh obtained with three velocity fields (green) and an additional, less smooth velocity field (blue).

Finally, we apply the four velocity field registration to the left hemisphere mesh to illustrate the limitations of the algorithm. An exemplary slice of the surface of the resulting mesh without post-processing is shown in the left of Fig. 8. Despite the fact that the four-velocity field deformation registers the image well (cf. center panel in Fig. 4), the deformed mesh does not match the complex cortical folding pattern. Furthermore, the (fourth) mesh deformation yields a jagged surface as indicated with the blue arrows. Applying mesh post-processing (again, smoothing and isotropic remeshing as described in [52]) mitigates this issue as shown in the center of Fig. 8.

In the right panel, the figure also shows in white the brain surface `lh.pial` obtained with the FreeSurfer `recon-all` command run on the MRI from “Ernie”. It can be seen that this surface matches the cortical folding better in comparison to the mesh deformed by our algorithm.

7. Discussion and Outlook. A novel approach to perform nonlinear image registration by solving a (sequence of) PDE constrained optimization problems has been considered. The efficacy of the approach has been presented by numerical results for brain image registration. Our volumetric registration algorithm obtains image registration comparable to surface and volumetric based registration [59].

As a proof of concept and first step, we focused on the ventricular system including the cerebral aqueduct. The presented results are promising and we are able to obtain a volume mesh that matches the ventricular system of the target subject from a manually crafted mesh matching the input subject.

We also show limitations of the algorithm in its current formulation when deforming a mesh for the left hemisphere. The hyperparameter tuning required to obtain accurate registration of the cortical folding patterns comes at the cost of introducing spikes when deforming the input mesh. We demonstrate that this issue can be fixed by post-processing the mesh. However, the deformed mesh does not match all cortical folds perfectly. This indicates that it might be necessary to combine our algorithm with surface-based registration as in [59].

Our numerical implementation is based on the established and user friendly Python library FEniCS. This implementation, while easy to read and modify, does currently not make use of the full potential of the DG scheme to be parallelized more efficiently than, e.g., CG schemes.

Besides providing a high performance implementation of the presented algorithm, it can also be enhanced in several regards. On the one hand, the influence of the choice of the regularity of the velocity

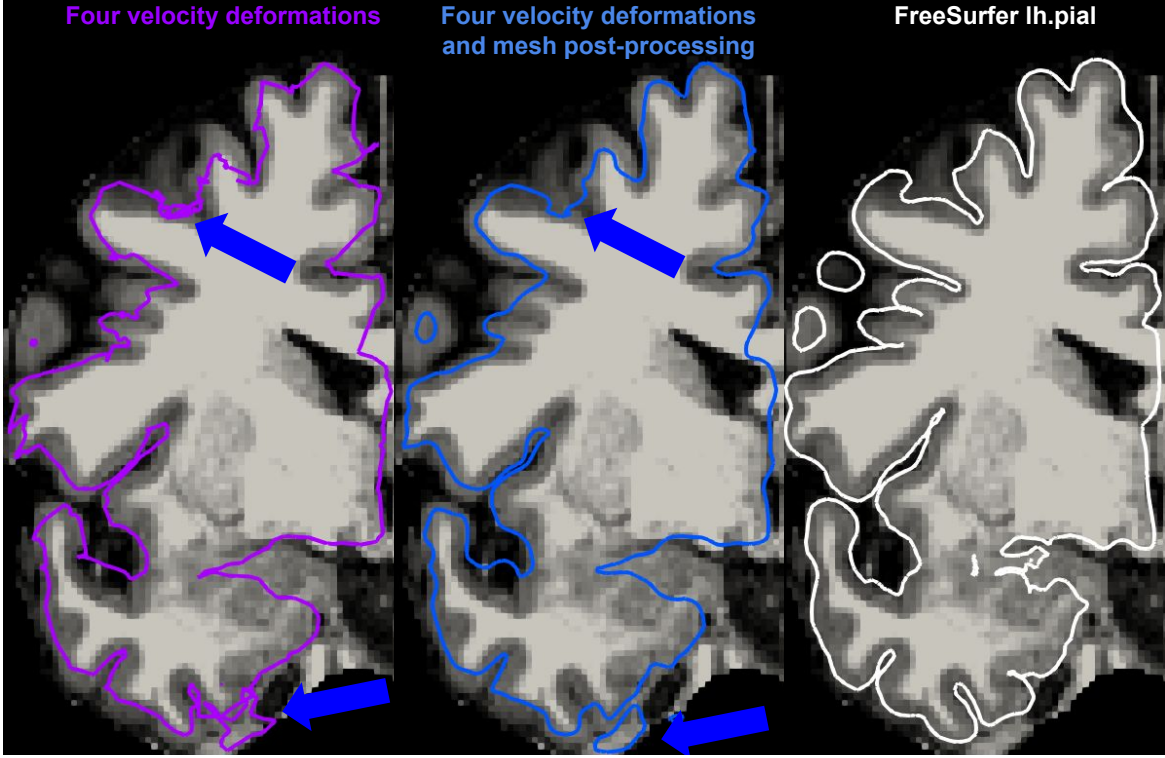


FIGURE 8. Background images: left hemisphere slice of the target MRI “Ernie”. In color: slices of the surface of the deformed template mesh obtained with four velocity fields before (violet, left) and after (blue, center) post-processing. Right: Surface *lh.pial* obtained with FreeSurfer *recon-all* (white). Blue arrows indicate that the mesh post-processing fixes artifacts induced by the mesh deformation.

field can be investigated. On the other hand, the approach can be translated into a neural network based approach based on, e.g., MeshGraphNets [58]. Hence, our approach can be combined with an implementation in GPU-accelerated frameworks and represents an algorithm, which bridges the gap between machine learning approaches and classical PDE-based approaches in image registration.

Acknowledgments. This research has been supported by the Research Council of Norway under the grants 300305 and 320753 and the German Academic Exchange Service (DAAD) under grant 57570343 of the program “Programm des projektbezogenen Personenaustauschs Norwegen 2021-2023”. This work has also been supported in part by the German Research Foundation (DFG) grant 314150341 of the priority program SPP1962. The computations presented in this work have been performed on the Experimental Infrastructure for Exploration of Exascale Computing (eX3), which is financially supported by the Research Council of Norway under contract 270053. The work was initiated during a workshop at the Simula cabin in Geilo, Norway. The authors wish to explicitly thank all of the respective institutions.

The authors also wish to thank Axel Kröner, Simon Funke and Kathrin Völkner for their discussions and feedback on writing the grant proposal and during the workshop in Geilo, respectively.

REFERENCES

- [1] Martin Alnæs, Jan Blechta, Johan Hake, August Johansson, Benjamin Kehlet, Anders Logg, Chris Richardson, Johannes Ring, Marie E Rognes, and Garth N Wells. The fenics project version 1.5. *Archive of Numerical Software*, 3(100), 2015.
- [2] Luigi Ambrosio. Transport equation and cauchy problem for bv vector fields. *Inventiones mathematicae*, 158(2):227, 2004.
- [3] Karm Veer Arya, Phalguni Gupta, Prem Kumar Kalra, and Pabitra Mitra. Image registration using robust m-estimators. *Pattern Recognition Letters*, 28(15):1957–1968, 2007.
- [4] M Faisal Beg, Michael I Miller, Alain Trouvé, and Laurent Younes. Computing large deformation metric mappings via geodesic flows of diffeomorphisms. *International journal of computer vision*, 61:139–157, 2005.
- [5] Laura Bojarskaite, Alexandra Vallet, Daniel M. Bjørnstad, Kristin M. Gullestad Binder, Céline Cunen, Kjell Heuser, Miroslav Kuchta, Kent-Andre Mardal, and Rune Enger. Sleep cycle-dependent vascular dynamics

in male mice and the predicted effects on perivascular cerebrospinal fluid flow and solute transport. *Nature communications*, 14(1):953, 2023.

[6] Wietse M Boon, Martin Hornkjøl, Miroslav Kuchta, Kent-Andre Mardal, and Ricardo Ruiz-Baier. Parameter-robust methods for the biot–stokes interfacial coupling without lagrange multipliers. *Journal of Computational Physics*, 467:111464, 2022.

[7] Alfio Borzi, Kazufumi Ito, and Karl Kunisch. Optimal control formulation for determining optical flow. *SIAM journal on scientific computing*, 24(3):818–847, 2003.

[8] Christian Brandenburg, Florian Lindemann, Michael Ulbrich, and Stefan Ulbrich. A continuous adjoint approach to shape optimization for navier stokes flow. In *Optimal control of coupled systems of partial differential equations*, pages 35–56. Springer, 2009.

[9] Lisa Gottesfeld Brown. A survey of image registration techniques. *ACM computing surveys (CSUR)*, 24(4):325–376, 1992.

[10] Malte Brunn, Naveen Himthani, George Biros, Miriam Mehl, and Andreas Mang. Fast gpu 3d diffeomorphic image registration. *Journal of parallel and distributed computing*, 149:149–162, 2021.

[11] Marius Causemann, Vegard Vinje, and Marie E Rognes. Human intracranial pulsatility during the cardiac cycle: a computational modelling framework. *Fluids and Barriers of the CNS*, 19(1):1–17, 2022.

[12] Elena Celledoni, Helge Glöckner, Jørgen Riseth, and Alexander Schmeding. Deep learning of diffeomorphisms for optimal reparametrizations of shapes, 2022.

[13] Kanglin Chen and Dirk A Lorenz. Image sequence interpolation using optimal control. *Journal of Mathematical Imaging and Vision*, 41:222–238, 2011.

[14] Xuxin Chen, Ximin Wang, Ke Zhang, Kar-Ming Fung, Theresa C Thai, Kathleen Moore, Robert S Mannel, Hong Liu, Bin Zheng, and Yuchen Qiu. Recent advances and clinical applications of deep learning in medical image analysis. *Medical Image Analysis*, page 102444, 2022.

[15] James D Christensen. Normalization of brain magnetic resonance images using histogram even-order derivative analysis. *Magnetic resonance imaging*, 21(7):817–820, 2003.

[16] Bernardo Cockburn and Johnny Guzmán. Error estimates for the runge–kutta discontinuous galerkin method for the transport equation with discontinuous initial data. *SIAM Journal on Numerical Analysis*, 46(3):1364–1398, 2008.

[17] Mattia Corti, Paola F Antonietti, Luca Dede, and Alfio Maria Quarteroni. Numerical modelling of the brain poromechanics by high-order discontinuous galerkin methods. *arXiv preprint arXiv:2210.02272*, 2022.

[18] Gianluca Crippa. *The flow associated to weakly differentiable vector fields*. PhD thesis, University of Zurich, 2008.

[19] Camillo De Lellis. Ordinary differential equations with rough coefficients and the renormalization theorem of ambrosio [after ambrosio, diperna, lions]. *Astérisque*, 317(972):175–203, 2008.

[20] Klaus Deckelnick, Philip J Herbert, and Michael Hinze. A novel $w^{1,\infty}$ approach to shape optimisation with lipschitz domains. *ESAIM: Control, Optimisation and Calculus of Variations*, 28:2, 2022.

[21] Michel C Delfour and J-P Zolésio. *Shapes and geometries: metrics, analysis, differential calculus, and optimization*. SIAM, 2011.

[22] Daniele Antonio Di Pietro and Alexandre Ern. *Mathematical aspects of discontinuous Galerkin methods*, volume 69. Springer Science & Business Media, 2011.

[23] Ronald J DiPerna and Pierre-Louis Lions. Ordinary differential equations, transport theory and sobolev spaces. *Inventiones mathematicae*, 98(3):511–547, 1989.

[24] Paul Dupuis, Ulf Grenander, and Michael I Miller. Variational problems on flows of diffeomorphisms for image matching. *Quarterly of applied mathematics*, pages 587–600, 1998.

[25] Patrick E Farrell, David A Ham, Simon W Funke, and Marie E Rognes. Automated derivation of the adjoint of high-level transient finite element programs. *SIAM Journal on Scientific Computing*, 35(4):C369–C393, 2013.

[26] Michael Fischer, Florian Lindemann, Michael Ulbrich, and Stefan Ulbrich. Fréchet differentiability of unsteady incompressible navier–stokes flow with respect to domain variations of low regularity by using a general analytical framework. *SIAM Journal on Control and Optimization*, 55(5):3226–3257, 2017.

[27] Bruce Fischl. Freesurfer. *Neuroimage*, 62(2):774–781, 2012.

[28] Karl J Friston, John Ashburner, Christopher D Frith, J-B Poline, John D Heather, and Richard SJ Frackowiak. Spatial registration and normalization of images. *Human brain mapping*, 3(3):165–189, 1995.

[29] Yabo Fu, Yang Lei, Tonghe Wang, Walter J Curran, Tian Liu, and Xiaofeng Yang. Deep learning in medical image registration: a review. *Physics in Medicine & Biology*, 65(20):20TR01, 2020.

[30] Eldad Haber and Jan Modersitzki. Numerical methods for volume preserving image registration. *Inverse problems*, 20(5):1621, 2004.

[31] Grant Haskins, Uwe Kruger, and Pingkun Yan. Deep learning in medical image registration: a survey. *Machine Vision and Applications*, 31:1–18, 2020.

[32] J. Haubner, M. Siebenborn, and M. Ulbrich. A continuous perspective on shape optimization via domain transformations. *SIAM Journal on Scientific Computing*, 43(3):A1997–A2018, January 2021.

[33] Karl Erik Holter, Benjamin Kehlet, Anna Devor, Terrence J Sejnowski, Anders M Dale, Stig W Omholt, Ole Petter Ottersen, Erlend Arnulf Nagelhus, Kent-André Mardal, and Klas H Pettersen. Interstitial solute transport in 3d reconstructed neuropil occurs by diffusion rather than bulk flow. *Proceedings of the National Academy of Sciences*, 114(37):9894–9899, 2017.

[34] Martin Hornkjøl, Lars Magnus Valnes, Geir Ringstad, Marie E Rognes, Per Kristian Eide, Kent-André Mardal, and Vegard Vinje. Csf circulation and dispersion yield rapid clearance from intracranial compartments. *bioRxiv*, pages 2022–05, 2022.

[35] Peter J Huber. Robust estimation of a location parameter. *Breakthroughs in statistics: Methodology and distribution*, pages 492–518, 1992.

[36] Philipp Jarde and Michael Ulbrich. Existence of minimizers for optical flow based optimal control problems under mild regularity assumptions. *Control and Cybernetics*, 48, 2019.

[37] Philipp Paul Jarde. *Analysis of optimal control problems for the optical flow equation under mild regularity*

assumptions. PhD thesis, Technische Universität München, 2018.

[38] Tamas I Jozsa, Jan Petr, Frederik Barkhof, Stephen J Payne, and Henk JMM Mutsaerts. Mri-based computational model generation for cerebral perfusion simulations in health and ischaemic stroke. *bioRxiv*, pages 2022–09, 2022.

[39] Bilge Karaçali and Christos Davatzikos. Estimating topology preserving and smooth displacement fields. *IEEE Transactions on Medical Imaging*, 23(7):868–880, 2004.

[40] CT Kelley and EW Sachs. Quasi-newton methods and unconstrained optimal control problems. *SIAM Journal on Control and Optimization*, 25(6):1503–1516, 1987.

[41] Douglas H Kelley, Tomas Bohr, Poul G Hjorth, Sebastian C Holst, Sabina Hrabětová, Vesa Kiviniemi, Tuomas Lilius, Iben Lundgaard, Kent-Andre Mardal, Erik A Martens, et al. The glymphatic system: Current understanding and modeling. *Iscience*, page 104987, 2022.

[42] Moritz Keuthen. *Second order shape optimization with geometric constraints*. PhD thesis, Technische Universität München, 2015.

[43] Ali R Khan, Lei Wang, and Mirza Faisal Beg. Freesurfer-initiated fully-automated subcortical brain segmentation in mri using large deformation diffeomorphic metric mapping. *Neuroimage*, 41(3):735–746, 2008.

[44] Arno Klein, Jesper Andersson, Babak A Ardekani, John Ashburner, Brian Avants, Ming-Chang Chiang, Gary E Christensen, D Louis Collins, James Gee, Pierre Hellier, et al. Evaluation of 14 nonlinear deformation algorithms applied to human brain mri registration. *Neuroimage*, 46(3):786–802, 2009.

[45] Sunil Koundal, Rena Elkin, Saad Nadeem, Yuechuan Xue, Stefan Constantinou, Simon Sanggaard, Xiaodan Liu, Brittany Monte, Feng Xu, William Van Nostrand, et al. Optimal mass transport with lagrangian workflow reveals advective and diffusion driven solute transport in the glymphatic system. *Scientific reports*, 10(1):1990, 2020.

[46] Dong C Liu and Jorge Nocedal. On the limited memory bfgs method for large scale optimization. *Mathematical programming*, 45(1):503–528, 1989.

[47] Jianfang Lu, Yong Liu, and Chi-Wang Shu. An oscillation-free discontinuous galerkin method for scalar hyperbolic conservation laws. *SIAM Journal on Numerical Analysis*, 59(3):1299–1324, 2021.

[48] Andreas Mang and George Biros. An inexact newton–krylov algorithm for constrained diffeomorphic image registration. *SIAM journal on imaging sciences*, 8(2):1030–1069, 2015.

[49] Andreas Mang, Amir Gholami, Christos Davatzikos, and George Biros. Pde-constrained optimization in medical image analysis. *Optimization and Engineering*, 19(3):765–812, 2018.

[50] Andreas Mang, Amir Gholami, Christos Davatzikos, and George Biros. Claire: A distributed-memory solver for constrained large deformation diffeomorphic image registration. *SIAM Journal on Scientific Computing*, 41(5):C548–C584, 2019.

[51] Kent-Andre Mardal, Marie E Rognes, Travis B. Thompson, and Lars Magnus Valnes. Software for mathematical modeling of the human brain - from magnetic resonance images to finite element simulation, June 2021.

[52] Kent-André Mardal, Marie E Rognes, Travis B Thompson, and Lars Magnus Valnes. Mathematical modeling of the human brain: From magnetic resonance images to finite element simulation, 2022.

[53] Jan Modersitzki. *FAIR: flexible algorithms for image registration*. SIAM, 2009.

[54] François Murat and Jacques Simon. Etude de problèmes d'optimal design. In *IFIP Technical Conference on Optimization Techniques*, pages 54–62. Springer, 1975.

[55] László G Nyúl and Jayaram K Udupa. On standardizing the mr image intensity scale. *Magnetic Resonance in Medicine: An Official Journal of the International Society for Magnetic Resonance in Medicine*, 42(6):1072–1081, 1999.

[56] László G Nyúl, Jayaram K Udupa, and Xuan Zhang. New variants of a method of mri scale standardization. *IEEE transactions on medical imaging*, 19(2):143–150, 2000.

[57] Francisco PM Oliveira and Joao Manuel RS Tavares. Medical image registration: a review. *Computer methods in biomechanics and biomedical engineering*, 17(2):73–93, 2014.

[58] Tobias Pfaff, Meire Fortunato, Alvaro Sanchez-Gonzalez, and Peter W Battaglia. Learning mesh-based simulation with graph networks. *arXiv preprint arXiv:2010.03409*, 2020.

[59] Gheorghe Postelnicu, Lilla Zollei, and Bruce Fischl. Combined volumetric and surface registration. *IEEE transactions on medical imaging*, 28(4):508–522, 2008.

[60] Jacob C Reinhold, Blake E Dewey, Aaron Carass, and Jerry L Prince. Evaluating the impact of intensity normalization on MR image synthesis. In *Medical Imaging 2019: Image Processing*, volume 10949, page 109493H. International Society for Optics and Photonics, 2019.

[61] Martin Reuter, H Diana Rosas, and Bruce Fischl. Highly accurate inverse consistent registration: a robust approach. *Neuroimage*, 53(4):1181–1196, 2010.

[62] Lars Ruthotto and Eldad Haber. Deep neural networks motivated by partial differential equations. *Journal of Mathematical Imaging and Vision*, 62:352–364, 2020.

[63] Jakob Schreiner and Kent-Andre Mardal. Simulating epileptic seizures using the bidomain model. *Scientific Reports*, 12(1):10065, 2022.

[64] Tobias Schwedes, David A Ham, Simon W Funke, Matthew D Piggott, Tobias Schwedes, David A Ham, Simon W Funke, and Matthew D Piggott. *Mesh dependence in PDE-constrained optimisation*. Springer, 2017.

[65] Mohak Shah, Yiming Xiao, Nagesh Subbanna, Simon Francis, Douglas L Arnold, D Louis Collins, and Tal Arbel. Evaluating intensity normalization on mr images of human brain with multiple sclerosis. *Medical image analysis*, 15(2):267–282, 2011.

[66] Chi-Wang Shu. Discontinuous galerkin methods for time-dependent convection dominated problems: Basics, recent developments and comparison with other methods. *Building bridges: connections and challenges in modern approaches to numerical partial differential equations*, pages 371–399, 2016.

[67] Aristeidis Sotiras, Christos Davatzikos, and Nikos Paragios. Deformable medical image registration: A survey. *IEEE transactions on medical imaging*, 32(7):1153–1190, 2013.

[68] Xiaofei Sun, Lin Shi, Yishan Luo, Wei Yang, Hongpeng Li, Peipeng Liang, Kuncheng Li, Vincent CT Mok,

Winnie CW Chu, and Defeng Wang. Histogram-based normalization technique on human brain magnetic resonance images from different acquisitions. *Biomedical engineering online*, 14(1):1–17, 2015.

[69] The CGAL Project. *CGAL User and Reference Manual*. CGAL Editorial Board, 5.5.1 edition, 2022.

[70] Alain Trouvé. Diffeomorphisms groups and pattern matching in image analysis. *International journal of computer vision*, 28(3):213–221, 1998.

[71] John Wilder Tukey. A survey of sampling from contaminated distributions. *Contributions to probability and statistics*, pages 448–485, 1960.

[72] Lars Magnus Valnes, Sebastian K Mitzsch, Geir Ringstad, Per Kristian Eide, Simon W Funke, and Kent-Andre Mardal. Apparent diffusion coefficient estimates based on 24 hours tracer movement support glymphatic transport in human cerebral cortex. *Scientific reports*, 10(1):1–12, 2020.

[73] Lars Magnus Valnes and Jakob Schreiber. Svmtk: Surface volume meshing tool kit, 2022.

[74] John C Vardakis, Liwei Guo, Dean Chou, and Yiannis Ventikos. Using multicompartmental poroelasticity to explore brain biomechanics and cerebral diseases. In *Advances in Critical Flow Dynamics Involving Moving/Deformable Structures with Design Applications: Proceedings of the IUTAM Symposium on Critical Flow Dynamics involving Moving/Deformable Structures with Design applications, June 18-22, 2018, Santorini, Greece*, pages 151–163. Springer, 2021.

[75] Pauli Virtanen, Ralf Gommers, Travis E Oliphant, Matt Haberland, Tyler Reddy, David Cournapeau, Evgeni Burovski, Pearu Peterson, Warren Weckesser, Jonathan Bright, et al. Scipy 1.0: fundamental algorithms for scientific computing in python. *Nature methods*, 17(3):261–272, 2020.

[76] Laurent Younes. *Shapes and diffeomorphisms*, volume 171. Springer, 2010.

[77] Daoping Zhang and Ke Chen. A novel diffeomorphic model for image registration and its algorithm. *Journal of Mathematical Imaging and Vision*, 60(8):1261–1283, April 2018.

[78] Qiang Zhang and Chi-Wang Shu. Error estimates for the third order explicit runge-kutta discontinuous galerkin method for a linear hyperbolic equation in one-dimension with discontinuous initial data. *Numerische Mathematik*, 126(4):703–740, 2014.

[79] Jean-Paul Zolésio. *Identification de domaines par déformations*. PhD thesis, Université de Nice, 1979.

[80] Jean-Paul Zolésio. The material derivative (or speed) method for shape optimization. *Optimization of distributed parameter structures*, 2:1089–1151, 1981.